Catalysis Today 334 (2019) 231–242

Contents lists available at ScienceDirect

Catalysis Today

journal homepage: www.elsevier.com/locate/cattod

Generalized approach for the synthesis of silica supported Pd-Zn, Cu-Zn and Ni-Zn gamma brass phase nanoparticles

Anish Dasgupta[a], Eric K. Zimmerer[a], Randall J. Meyer[b], Robert M. Rioux[a,c,*]

[a] Department of Chemical Engineering, The Pennsylvania State University, PA 16802, USA
[b] ExxonMobil Research and Engineering, Annandale, NJ, 08801 USA
[c] Department of Chemistry, The Pennsylvania State University, PA 16802, USA

ARTICLE INFO

Keywords:
Intermetallic
Gamma brass
Pd-Zn
Ni-Zn
Ethylene hydrogenation
X-ray diffraction
X-ray absorption spectroscopy

ABSTRACT

The existing literature suggests it is particularly difficult to access the catalytically relevant, and relatively complex, intermetallic γ-brass crystal structure through traditional nanoparticle (NP) synthesis techniques. We introduce a simple and rational approach to access this phase in M-Zn (M = Pd, Cu, Ni) systems as silica-supported single-phase nanocrystals. This hybrid approach involves the initial synthesis of supported M/SiO_2 through traditional approaches (dry impregnation and strong electrostatic adsorption) followed by heating to high temperatures in the presence of a stoichiometric amount of metallic Zn in an evacuated closed system for several hours. We demonstrate the generality of this method with three different catalytically important bimetallic systems: Pd-Zn, Ni-Zn and Cu-Zn. Of these three, Pd-Zn is by the far the most popular in terms of catalytic applications and yields the smallest particle size (~8 nm). We tested the influence of various synthesis parameters on phase purity and particle size distribution in case of the synthesized γ-brass Pd-Zn/SiO_2 supported catalysts and provide general guidelines towards optimization of synthesis. Upon transformation of Pd/SiO_2 to γ-brass Pd-Zn/SiO_2, a precipitous drop in CO adsorption and a 25 kJ/mol increase in the ethylene hydrogenation barrier is observed, indicating the catalytic active sites are significantly modified as a result of alloying. We anticipate these catalysts may find applications in various Pd-catalyzed chemistries.

1. Introduction

A major focus in the field of heterogeneous catalysis is to design catalytic materials with increasing activity and selectivity [1–3]. The state-of-the-art is the synthesis of strategic bimetallic materials where the catalytic propensities of traditional active atoms (Pd, Ni, Pt) are modulated by the presence of a second metal (Zn, Ag, Bi) [4,5] due to electronic and geometric effects [3,6,7]. Crystalline bimetallic catalysts are typically of two types: (i) alloys and (ii) intermetallics (although other significantly more complex multi-metallic catalysts, often employing specific core-shell or porous architecture are present in recent literature [8–15]). Intermetallics have well-defined and periodic atomic site occupancy whereas alloys are randomly substituted solid solutions. This essentially means any bulk measure related to active site geometry (such as x-ray absorption spectroscopy (XAS), CO-FTIR, etc.) in the case of alloys is an average over millions of unit cells whereas for an intermetallic the values are intrinsic to each unit cell, making intermetallic compounds excellent model systems for studying catalytic structure-function correlations [16].

Innumerable bimetallic catalysts (both alloy and intermetallic) have been examined for a large variety of chemistries and are often found to outperform their monometallic counterparts. For example, Pd-Ag alloys are the industrial standard for acetylene semi-hydrogenation in an ethylene rich stream since the inclusion of Ag has a huge positive impact on the ethylene selectivity compared to pure Pd [17]. Ni-Ga intermetallic catalysts have better selectivity during hydrogenation [18–20] and improved ability for CO_2 reduction to methanol and hydrocarbons [21,22] compared to pure Ni. Pt-Sn catalysts have excellent hydrocarbon dehydrogenation ability for light alkanes [23–25]. Several Pt-M catalysts are proposed as better formic acid dehydrogenation catalysts since they have significantly lower selectivity to CO (in favor of CO_2) and are more active than Pt [26–29]. Pt-M catalysts show better activity compared to Pt for the electrocatalytic reduction of oxygen and serves as superior cathodes for low temperature fuel cells [30,31].

Of all bimetallic systems, one of the most widely studied are the M-Zn materials where M is typically a *d*-block element such as Ni, Cu, Pt or Pd. Zn can form a large number of alloys and intermetallics with most *p*- and *d*-block elements and its inclusion can often improve catalytic

* Corresponding author at: Department of Chemical Engineering, The Pennsylvania State University, PA 16802, USA
E-mail address: rioux@engr.psu.edu (R.M. Rioux).

https://doi.org/10.1016/j.cattod.2018.10.050
Received 16 July 2018; Received in revised form 15 October 2018; Accepted 19 October 2018
Available online 29 October 2018
0920-5861/

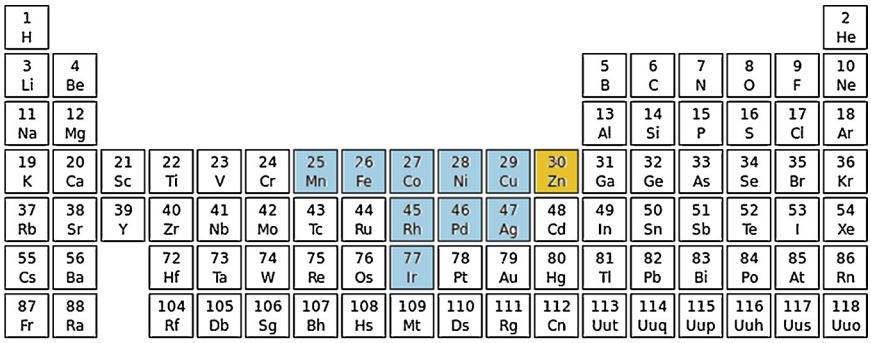

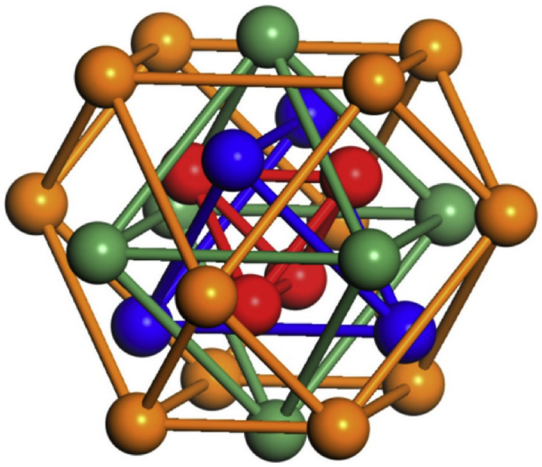

Fig. 1. (top) Elements which form γ-brass phase with Zn (marked in blue). (bottom) Illustration of the sites in the γ-brass structure: inner tetrahedral (IT, red), outer tetrahedral (OT, blue), octahedral (OH, green), and cuboctahedral (CO, orange). Reprinted with permission from reference [49], copyright 2017, American Chemical Society. (For interpretation of the references to colour in this figure legend, the reader is referred to the web version of this article.)

performance for a wide range of chemistries. For example, Pd-Zn is one of the most widely studied catalysts for methanol steam reforming [32]. Pd-Zn is also effective for partial methanol oxidation, methanol dehydrogenation, acetylene and butadiene semi-hydrogenation and ester hydrogenation [33–37]. Ni-Zn catalysts find application for semi-hydrogenation [38], selective dehydrogenation [39], and other potentially useful chemistries such as hydrazine oxidation [40] and synthesis of 2,5 dimethylfuran [41]. Pt-Zn has been tested by Miura et al. to be a more effective formic acid dehydrogenation catalyst than Pt [42].

Typically, all Zn based catalysts reported in literature are of the form M_3Zn (α phase) or M_1Zn_1 (β phase) [30,36,42–45]. The α-phase is an alloy (random substituted solid solution) and is often visualized as an FCC cell (similar to the majority element M) where one of the four atoms in the unit cell is replaced by Zn [43,46] while the β-phase typically has a tetragonal unit cell and its active surface is modeled as alternating M and Zn atoms [36,38,43,46]. However, Zn is also known to form a very stable, Zn-rich, γ-brass phase with a wide range of catalytically relevant metals (Fig. 1) which has received less attention in the catalytic community [47]. This phase is an intermetallic and has a large (~0.9 nm) 52 atom unit cell which crystallizes as the I-43 m space group. The unit cell is described as 2 interpenetrating 26-atom polyhedrons at (0, 0, 0) and (0.5, 0.5, 0.5) [48]. One such polyhedron is illustrated in Fig. 1. The crystal structure has four symmetrically inequivalent lattice sites – inner tetrahedral (IT, multiplicity of 8/unit cell), outer tetrahedral (OT, multiplicity of 8/unit cell), octahedral (OH, multiplicity of 12/unit cell) and cuboctahedral (CO, multiplicity of 24/unit cell) [48].

The γ-brass phase is thermodynamically stable and easily accessed by traditional high temperature diffusion synthesis [50–53]. Despite having obvious advantages such as exceptional composition control and exclusion of support effects [54], the major drawback of this traditional synthesis approach is that the particle size is typically on the order of microns, and have a surface area of only ~1 m^2/g. This low surface area makes the materials unappealing for commercial catalytic applications. In this publication, we will demonstrate the γ-brass phase can be synthesized at a catalytically-relevant particle size ($d \leq 10$ nm) in a supported form through a simple two-step approach.

Very few reports exist where the γ-brass phase has been accessed in the form of catalytically relevant high surface area NPs [55,56] even though it may have significant catalytic implications because of its unique, periodic crystal structure and ability to create isolated (including single atom [49]) active sites. For example, Spanjers et al. reported the bulk Ni-Zn γ-brass phase is about twice as selective for acetylene semi-hydrogenation as the corresponding β or α bulk phases possibly due to an increase in the Ni-Ni distance in the crystal lattice [38].

Cable and Schaak [55] synthesized the prototypical Cu_5Zn_8 γ-brass NPs with a bimodal particle size distribution with the majority of the metal mass forming relatively large particles (~70 nm). A notable disadvantage of this synthetic protocol is that an initial (nominal) composition of Cu:Zn = 1:8 is required to obtain a final composition of Cu:Zn = 5:8; there was no logical explanation for this stoichiometric mismatch. This clearly highlights colloidal synthesis approaches lack generality for extension to other M-Zn γ-brass bimetallic systems. On the other hand, using a traditional bulk synthesis approach, Mukhopadhyay et al. [56] synthesized a large Cu_5Zn_8 ingot from a stoichiometric starting composition and optimized the subsequent ball milling step. However, utilizing this approach, the particle size could not be reduced below ~150 nm even after several days of ball milling. To our knowledge, no literature is available regarding the synthesis of Pd-Zn or Ni-Zn γ-brass phase as supported NPs. It was found that even when a sufficiently large Zn source is present to stoichiometrically form the γ-brass phase only the β phase could be achieved for both Pd-Zn [36,37,55,57,58] and Ni-Zn [44,45] through established synthesis

approaches.

In the current paper, we introduce a simple yet effective approach to reliably access γ-brass phase NPs supported on silica. We demonstrate the same synthesis principle extends to three different M-Zn systems: Pd-Zn, Ni-Zn and Cu-Zn. Our synthesis bears conceptual similarities with the methods introduced by Miura et al. [42] and (to a lesser extent) Onda et al [59] (see Section S1 for comparison). However, to our knowledge this work represents the first successful synthesis of silica-supported M-Zn γ-brass catalysts through a generalized approach. We have not extended the current work to other refractory or reducible oxides; therefore, the application of our approach may potentially be limited to silica. The reactivity difference between Zn with M versus the support will dictate the success, and therefore extension of the method to other supports.

Of the three M-Zn systems examined in this work, we focused a majority of our efforts on the Pd-Zn system since it yielded the smallest γ-brass particles and has the highest catalytic relevance of the three synthesized M-Zn intermetallics. We present a parametric study of the various synthesis parameters to reduce the Pd-Zn particle size to < 10 nm, close to the state-of-the-art for such well-defined intermetallic nanocrystals [16].

2. Experimental section

2.1. Synthesis of M-Zn/SiO_2 γ-brass NPs

2.1.1. Step 1: synthesis of M/SiO_2 NPs

A SiO_2 (Sigma Aldrich, Davisil Grade 62, 60–200 mesh) supported monometallic catalyst was synthesized initially through two different synthesis techniques – dry impregnation (DI) and strong electrostatic adsorption (SEA). For DI, an aqueous solution of the appropriate precursor (ammonium tetrachloropalladate ($(NH_4)_2PdCl_4$, Alfa Aesar), tetraaminepalladium chloride ($Pd(NH_3)_4Cl_2$, Alfa Aesar), copper sulphate hemipentahydrate ($CuSO_4{\cdot}2.5H_2O$, Sigma Aldrich), nickel nitrate hexahydrate ($Ni(NO_3)_2{\cdot}6H_2O$, Sigma Aldrich) or iridium trichloride ($IrCl_3$, Sigma Aldrich)) was added dropwise to the silica gel along with periodic mixing until the powder attained a wet clay texture (i.e., incipient point) and then dried (in static air) for 40 min at 110 °C. The concentration of the solution was intentionally made such that this process needed to be repeated 3× to reach the desired loading (5% or 9%). The relatively high weight loading allows for easy characterization and confirmation the desired phase-pure γ-brass phase NPs formed. After impregnation, samples were dried overnight at 110 °C in static air and then calcined and reduced (~150 mL/min) in a tube furnace (Thermo Scientific) according to one of the following two protocols:

Protocol 1: Calcined in ultra-zero air (Praxair) for 5 h at 700 °C followed by reduction in hydrogen (5% in Ar, Praxair) for 2 h at the same temperature. A slow heating ramp of 1 °C/min up to the set point of 700 °C was used.

Protocol 2: Calcined in ultra-zero air (Praxair) for 5 h at 400 °C followed by reduction in 5% hydrogen for 2 h at 250 °C. A heating ramp of ~1.7 °C/min was utilized to reach the set point of 400 °C. The furnace was naturally cooled from 400 °C to 250 °C after the calcination step.

Unless otherwise mentioned Protocol 1 has been used in this manuscript.

For SEA synthesis, tetraaminepalladium chloride was used as the precursor and the pH of the aqueous solution was adjusted to ~11 before addition of the support [60]. The pH was maintained by dropwise addition of either 0.5 or 1.5 M NaOH solution and measured with a calibrated pH meter (Thermo Scientific). We pretreated catalysts synthesized by the SEA method using Protocol 2.

2.1.2. Step 2: Zn Inclusion to form γ-brass M-Zn silica-supported catalysts

The material (M/SiO_2) prepared in Step 1 is mixed with a stoichiometric amount (Pd:Zn = 0.19 atomic ratio) of metallic Zn (Alfa Aesar, 99.9%) and loaded in alumina crucibles (LSP Ceramics). The crucibles are plugged with a small amount of quartz wool (Technical Glass Products) and placed inside homemade quartz ampoules. Ampoules were evacuated to ~50 mTorr and sealed using a flame torch. The evacuated ampoules are then heated to 750 °C in a box furnace (Thermo Scientific Lindberg Blue M) for 12 h (unless otherwise mentioned, see Section 3.2). The choice of temperature is standard for thermal diffusion based bulk synthesis and provides a sufficiently large Zn vapor pressure (Figure S1) for sufficient Zn inclusion into M [38,49–51,53,61–63]. The materials thus synthesized are directly characterized without any further processing (calcination, reduction, etc.).

A Pd-free catalyst was prepared to provide an estimate for background reactivity during ethylene hydrogenation. Zn powder was added to as-purchased silica gel followed by heating for 72 h at 750 °C under vacuum (similar to Step 2). The ratio of silica to Zn was identical to that used for the 5% Pd/SiO_2 sample.

2.2. Synthesis of bulk Pd-Zn materials

Bulk Pd-Zn materials were synthesized as reference materials for x-ray absorption spectroscopy (XAS) analysis. We synthesized $Pd_{10}Zn_{42}$ (γ-brass) and PdZn (β) by heating stoichiometric amounts of metallic Pd (99.99% Alfa Aesar) and Zn granules (99.99% Sigma Aldrich) under vacuum at 750 °C for 24 h in the same set-up as the Step 2 of our NP synthesis. The resultant ingots were ground to powder in a Spex Sample Prep ball mill for 2 h under N_2 atmosphere and using Vertrel XF (Dupont) as a fluidizing agent. After milling, the materials were annealed under vacuum at 500°C for 3 days. X-ray diffractograms in Figure S2 provide evidence the desired phases were synthesized by the solid-state diffusion approach.

2.3. Characterization

2.3.1. X-ray Diffraction (XRD)

X-ray diffraction of the synthesized materials were performed on a PanAnalytical Empyrean instrument using Cu K_α radiation. The full experimental conditions are available in a previous publication from our group [49].

2.3.2. Inductively Coupled Plasma Optical Emission Spectrometry (ICP-OES)

Elemental Analysis was performed on an Agilent 700 series ICP-OES. The samples (~10-15 mg each) were dissolved in 1.8 mL HF and 3 mL freshly prepared aqua regia and the resultant solution was diluted to 16 mL in DI water prior to analysis. ICP-OES was performed on the M/SiO_2 materials (to calculate the required amount of Zn for Step 2 of the synthesis) and the synthesized bimetallics. The instrument was calibrated before each experiment with pure metal standards (1 mg/mL, High Purity Standards). Standards of different concentrations were prepared by diluting the commercial stock solutions with a known amount of DI water. The linear regression of the standard calibration curves were used to calculate the metal concentration(s) of the synthesized (acid digested) samples.

2.3.3. Transmission Electron Microscopy (TEM) and Scanning Transmission Electron Microscopy-Energy Dispersive Spectroscopy (STEM-EDS)

Both TEM and STEM-EDS was performed on a FEI Talos microscope with an acceleration voltage of 200 kV. The samples were suspended in ethanol via sonication and then drop-cast on a Cu (or Mo when measuring Cu samples) grid. The sample-loaded grid was air dried overnight at room temperature and then further dried at 110 °C for ~20 min. For estimation of the average particle size and corresponding distribution, ~100 particles were counted in each case. The Fiji software package was used for this purpose [64].

2.3.4. CO Chemisorption

CO (99.99%, Airgas) chemisorption experiments were performed on a Micromeritics ASAP 2020 at 35 °C. For chemisorption experiments, Pd/SiO_2 (100 mg) and $Pd\text{-}Zn/SiO_2$ (250 mg) were dried at 120 °C for 2 h in He (UHP, Praxair) and then reduced at 250 °C for 5 h in H_2 (UHP, Praxair) *in-situ*. The reason for using a larger mass in case of the bimetallic sample is the anticipation that the particle size increases upon Zn inclusion resulting in a dilution of the surface Pd by Zn. The irreversible amount of CO chemisorbed onto the surface was determined as the difference in the CO uptake between the first (chemisoption + physisorption) and the repeat analysis (physisorption). A Pd:CO ratio of 1:1 is assumed to estimate the particle size from the irreversible uptake of CO [65].

2.3.5. X-ray Absorption Spectroscopy (XAS)

XAS experiments were performed at the Advanced Photon Source, Argonne National Laboratoryusing beamlines – 20-ID-B, 9-ID-B or 10-ID-B MRCAT. All spectra were collected by hand pressing the sample, appropriately diluted in silica or boron nitride (measurement of each sample and each edge required different amounts of dilution because of the difference in the metal loading), in a standard cylindrical "6-shooter" holder. Data was collected in transmission at both the Pd Kedge (24350 eV) and Zn K edge (9659 eV) with reference foils used for edge alignment. For each edge, data was typically acquired ~200 eV before the edge jump and up to ~1000 eV post-edge. The experimental data was analyzed using the Demeter software package [66,67] while employing a simultaneous fit of the k, k^2 and k^3 weighted Fourier transforms. Full details of the fitting procedure are provided in Section S3 of the Supporting Information.

2.3.6. X-ray photoelectron spectroscopy (XPS)

XPS experiments were performed using a Physical Electronics VersaProbe II instrument equipped with a monochromatic Al K_α x-ray source ($h\nu$ = 1486.7 eV) and a concentric hemispherical analyzer. Charge neutralization was performed using both low energy electrons (< 5 eV) and Ar ions. The binding energy axis was calibrated using sputter cleaned Cu (Cu $2p_{3/2}$ = 932.62 eV, Cu $3p_{3/2}$ = 75.1 eV) and Au foils (Au $4f_{7/2}$ = 83.96 eV) [68]. Peaks were charge referenced to CH_x band in the C 1 s spectra at 284.8 eV. Measurements were made at a takeoff angle of 45° with respect to the sample surface plane. Quantification was done using instrumental relative sensitivity factors (RSFs) that account for the x-ray cross section and inelastic mean free path of the electrons.

2.4. Catalytic ethylene hydrogenation (Proof of catalytic activity)

Ethylene hydrogenation is a sensitive probe reaction to demonstrate the modified (relative to Pd) catalytic behavior of the bimetallic Pd-Zn catalyst. γ-brass $Pd\text{-}Zn/SiO_2$ (15 mg, synthesized by SEA, calcination/reduction by Protocol 2) and 5% Pd/SiO_2 (13 mg of an approximately homogenous mixture of 5 mg Pd/SiO_2 and 1260 mg SiO_2) were reduced at 200 °C for 4 h in hydrogen (UHP) in a fritted tubular flow reactor (10 mm I.D., ChemGlass) and then held at that temperature for 20 min under He (UHP) to preclude effect of potential hydride formation on reaction kinetics.

The catalyst was cooled under He to the desired reaction temperature and equilibrated for 30 min before introduction of reactants. The reactant stream consisted of a mixture of ethylene (250 Torr, 99.99%, Praxair), hydrogen (250 Torr) and balance He. The total volumetric flow rate maintained by Tylan mass flow controllers was 30 mL/min. The effluent gas was analyzed online with an Agilent 7890 GC fitted with a GS-Alumina PLOT column (d = 0.5 mm, l = 30 m length). For each catalyst, an Arrhenius plot was constructed in the temperature range 30–45 °C. Differential conversion (< 10%) is ensured in each case. The first point is repeated at the end of the experiment to ensure the catalyst did not change over the course of the study.

During synthesis of the γ-brass Pd-Zn catalyst, we identified the formation of a Zn_2SiO_4 impurity (see Section 3.1 and 3.2). In order to confirm the measured reactivity for the hydrogenation of ethylene originates from Pd-Zn, we synthesized a sample containing only Zn_2SiO_4-ZnO supported on SiO_2 and tested its ethylene hydrogenation activity under the same reaction conditions mentioned above.

3. Results and discussion

3.1. Proof of synthesis of supported, phase-pure γ-brass NPs

We demonstrate the ability to synthesize phase-pure Pd-Zn γ-brass NPs through the method introduced above by initially focusing on the production of large NPs to enable more facile characterization and unequivocal identification of the γ-brass phase. Since our approach includes Zn addition to a preformed Pd particle, we intentionally used large(r) Pd NPs supported on silica to ensure we synthesized commensurately large $Pd\text{-}Zn/SiO_2$ NP (see section S2). We used a nominal Pd loading of 9 wt. % Pd/SiO_2 (determined to be 8.34% by ICP-OES) synthesized using ammonium tetrachloropalladate as the Pd precursor. After the inclusion of Zn, we initially characterized the supported catalyst by XRD (Fig. 2a). It is immediately obvious all Pd peaks from the Pd/SiO_2 starting material disappeared (Fig. 2a) and a completely unique phase formed due to the inclusion of Zn. The only crystalline phase detected after synthesis is the γ-brass Pd-Zn phase; the diffraction peaks for the γ-brass phase are sharp and well defined due to the large size of the Pd-Zn nanoparticles. As further confirmation, fast Fourier transform of the HR-TEM in Fig. 2b and c revealed the crystalline nature of the as-synthesized NPs. The diffraction spots can be indexed to the γ-brass Pd-Zn phase with the brightest spot corresponding to the (330) plane (d = 0.211 nm), consistent with the highest intensity XRD peak at 2θ ~42°.

The particle size distribution is unimodal having an average diameter of ~ 40 nm with a few significantly larger agglomerated particles identified (Fig. 2d). STEM-EDS (Fig. 2e) was utilized to identify the compositional distribution on a single particle basis. Fig. 2f demonstrates very little spread in the Pd:Zn ratio with the majority of the individual particles falling within the compositional bounds of the γ-brass phase (marked by black lines on Fig. 2f, Pd-Zn phase diagram presented in Figure S3). A STEM-EDS linescan (Figure S4) was performed along an arbitrarily chosen particle and the Pd:Zn ratio remained nearly constant along the entire diameter of the particle (d ~ 36 nm) supporting our XRD results that complete alloying has been achieved with no significant core-shell formation in the NPs. XRD failed to detect any impurity phases, but we detected a small amount of Zn_2SiO_4/ZnO in the form of highly dispersed particles on the support by STEM-EDS. Based on STEM-EDS quantification it is estimated to be ~0.5 mol % with respect to SiO_2 (Figure S5). There is no evidence from TEM observations (Fig. 2b) to suggest these Zn^{2+} impurities nucleate around or envelope the Pd-Zn particles. The Zn_2SiO_4 phase appears to be the result of a distinct side reaction between metallic Zn and the support which is significantly less favorable than the Pd alloying step since the majority of the Zn is included into Pd-Zn γ-brass phase. If a majority of the Zn preferred to either react with the SiO_2 or evaporate, we would not have achieved phase pure γ-brass NPs since we started with a stoichiometric amount of metallic Zn.

XAS can provide strong evidence of alloying as well as its catalytically relevant consequences — geometric and electronic effects. Table 1 summarizes the value of derived parameters describing the fitted EXAFS data (fits presented in Figure S6). The details of the fitting technique are presented in Section S3. Table 1 clearly demonstrates the γ-brass phase Pd-Zn has significantly lower Pd-Pd coordination in comparison to the Pd-Zn β-phase indicating the possibility of extreme Pd site-isolation in an inert Zn matrix.

Fig. 3 shows a comparison of the Pd *K*-edge XANES spectra of the bulk γ–$Pd_{10}Zn_{42}$, γ-$Pd\text{-}Zn/SiO_2$, β-PdZn and a Pd foil. The bimetallic

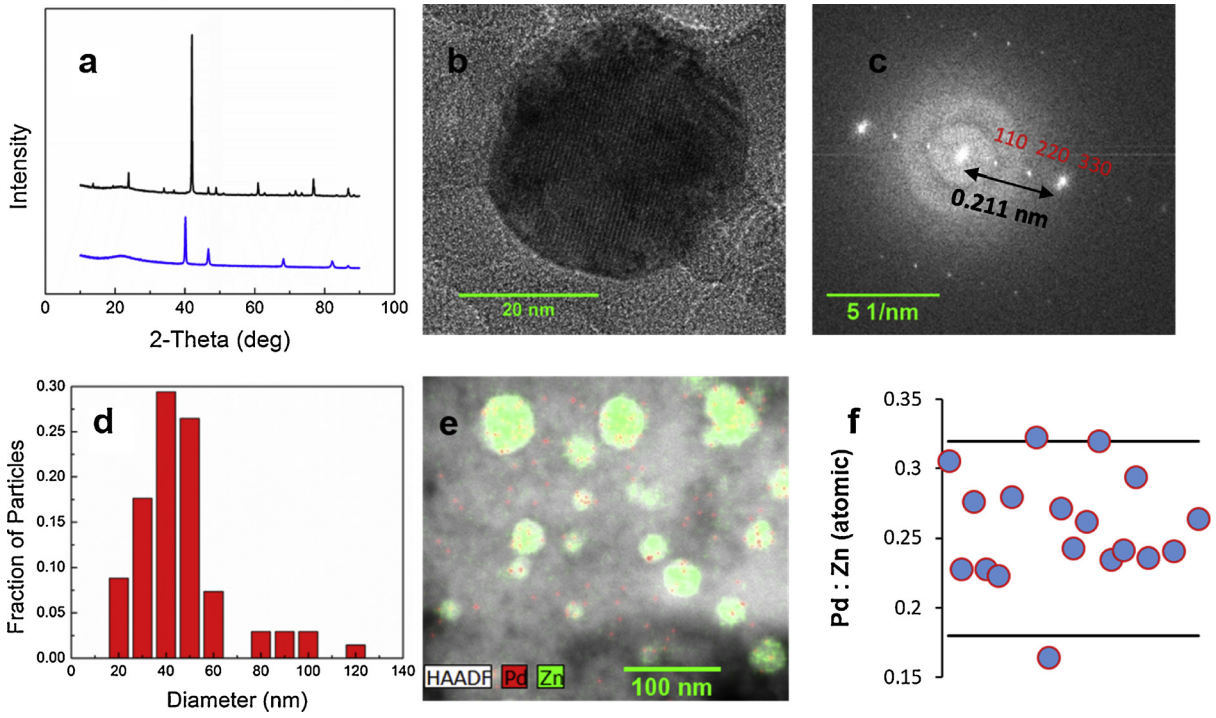

Fig. 2. (a) XRD pattern of γ-brass Pd-Zn/SiO_2 (black) and parent 9% Pd/SiO_2 before Zn inclusion (blue), (b) HR-TEM image, (c) FFT of HR-TEM image with the brightest spots indexed, (d) particle size distribution determined through TEM, (e) STEM-EDS elemental mapping of NPs and (f) individual particle Pd:Zn atomic ratio determined by STEM-EDS of as-synthesized γ-brass Pd-Zn/SiO_2 described in Section 3.1. All sharp XRD features in (a) match the γ-brass crystal structure. The spots in (c) match with the Pd-Zn γ-brass phase in terms of *d*-spacing reported in the ICDD PDF4 database. The two black lines in (f) indicate the compositional bounds (15.4–24 at% Pd, [47]) of the Pd-Zn γ-brass phase while each blue circle represents the composition of an individual NP. (For interpretation of the references to colour in this figure legend, the reader is referred to the web version of this article.)

Table 1
Fitted EXAFS parameters (coordination numbers interatomic distances and Debye Waller factors) for the bulk and NP Pd-Zn materials.

	γ–$Pd_{10}Zn_{42}$	γ-Pd-Zn/SiO_2	β–PdZn
CN[a] Pd-Zn	10.0 ± 0.9	9.4 ± 1.3	7.9 ± 0.3
CN Zn-Pd	3.6 ± 0.2	2.4 ± 0.3	7.9 ± 0.3
R[b] Pd-Zn	2.63 ± 0.01	2.63 ± 0.01	2.61 ± 0.002
σ^{2}[c] Pd-Zn	0.010 ± 0.001	0.011 ± 0.001	0.008 ± 0.0003
CN Pd-Pd	0.6 ± 0.5	1.0 ± 0.8	4.2 ± 1.1
R Pd-Pd	2.95 ± 0.02	2.95 ± 0.03	2.87 ± 0.01
σ^2 Pd-Pd	0.003 ± 0.003	0.006 ± 0.005	0.015 ± 0.003
CN Zn-Zn	5.1 ± 0.7	5.3 ± 1.9	2.5 ± 1.0
R Zn-Zn	2.64 ± 0.01	2.65 ± 0.01	2.90 ± 0.01
σ^2 Zn-Zn	0.010 ± 0.001	0.016 ± 0.004	0.010 ± 0.003
CN Pd total	10.6 ± 1.4	10.4 ± 2.1	12.1 ± 1.4
CN Zn total	8.7 ± 0.9	7.7 ± 2.2	10.4 ± 1.3
E0 Pd	0.95 ± 1.0	0.45 ± 1.7	−3.3 ± 0.6
E0 Zn	0.93 ± 0.4	0.64 ± 0.8	2.2 ± 0.3

[a] Coordination number.
[b] Interatomic distance in Å.
[c] Debye Waller factor.

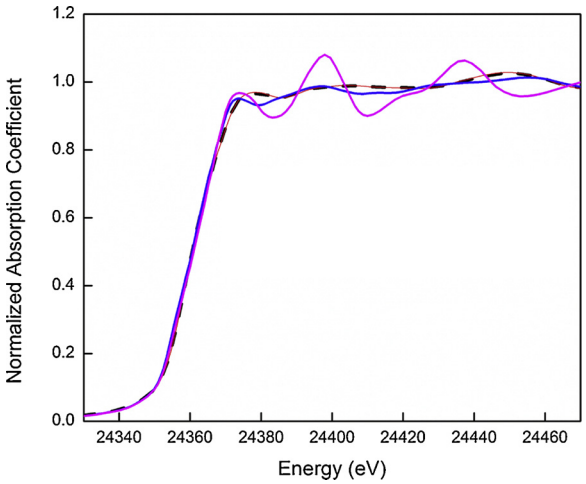

Fig. 3. XANES spectra of Pd foil (magenta line), Pd-Zn/SiO_2 γ-brass NPs (black dash line), bulk γ-$Pd_{10}Zn_{42}$ (red line) and bulk β-PdZn (blue line). (For interpretation of the references to colour in this figure legend, the reader is referred to the web version of this article.)

samples show strong perturbations from the Pd foil, indicating the formation of an alloy. The broadening of the features beyond the edge are also signatures of the hybridization changes (so called "electronic effect" [7]) in the bonding commonly associated with alloying [69]. Furthermore, the spectra of the supported γ-Pd-Zn/SiO_2 lies directly on γ–$Pd_{10}Zn_{42}$, strongly suggesting the supported material is of the same phase as the bulk material.

XPS was performed on the freshly prepared Pd-Zn/SiO_2 γ-brass material (Figure S7). Both Pd and Zn are present on the surface, but it is relatively enriched in Zn ($(Pd:Zn)_{surface} \sim 1:12$, $(Pd:Zn)_{bulk} \sim 1:5$). There may be different explanations for this apparent surface segregation. Our XPS instrument has no *in-situ* sample treatment with high vacuum sample transfer capability. As a result, samples were exposed to air which may have resulted in enriching the surface with Zn. Further, the Pd signal is quite small and suffers from interference with the much stronger O 1 s signal making accurate quantification difficult. In any case, it is well-known that surface composition may vary significantly under different reactive environments [70–73] and hence is not an intrinsic property of the catalyst, but should be evaluated under specific situations using highly specialized equipment such as Ambient Pressure-XPS (as discussed in the publications sited above). The Pd $3d_{5/2}$ peak is seen to be shifted by ~0.6 eV (to 335.7 eV) relative to the

standard Pd foil (335.1 eV). This shift does not overlap with either the formation of a Pd oxide (336.1–336.5 eV for PdO and 337.7–338.3 eV for PdO_2) or a Pd-Si compound (336.1–337 eV) [74] and hence may be attributed to an electronic effect of Zn alloying to Pd, consistent with our previous XANES experiments.

3.2. Effect of synthetic parameters on final bimetallic particle size

Our synthesis approach is a sequential combination of two well-known techniques – support impregnation with a metal precursor solution followed by a high temperature diffusion step to introduce Zn into pre-formed Pd NPs. This provides two distinct directions for parametric optimization as discussed below.

3.2.1. Control of Pd-Zn particle size based on parametric variation during the synthesis of Pd/SiO_2 (Step 1)

3.2.1.1. Metal loading. In this section, we examined the impact of metal loading on the final size of the Pd-Zn γ-brass phase NPs. We synthesized nominally 5% Pd/SiO_2 (actual weight loading of 4.4% by ICP) by DI using ammonium tetrachloropalladate. Protocol 1 was followed for the calcination-reduction steps for comparison with the 9% Pd/SiO_2 catalyst which previously served as a proof-of-principle material that nanoscale Pd-Zn γ-brass particles can form by our sequential synthetic approach. We added a stoichiometric amount of Zn and followed the high temperature synthesis (Step 2) procedure previously outlined. The synthesized material is phase pure Pd-Zn γ-brass as determined by XRD (Figure S8). We found the Pd-Zn particle size decreased as the Pd metal loading in the parent Step 1 material is reduced from 9 to 5% (note that if the Pd loading in the Step 1 material is reduced, the amount of Zn added in Step 2 is also proportionately reduced to maintain stoichiometric Pd:Zn ratio in each case). In particular, the Pd-Zn average diameter was ~40 nm when the Pd loading in the monometallic Step 1 material was 9% but the bimetallic particle size reduced to ~25 nm for the nominally 5% Pd/SiO_2 catalyst.

The as-synthesized 5% Pd/SiO_2 (synthesized by either DI or SEA) represents our standard catalyst (prepared according to the Step 1 preparation procedure) followed by impregnation with a stoichiometric amount of Zn. The reason for this is the weight loading of 4.3 wt. % (actual) of Pd was the maximum achievable with SEA which is important for comparison with catalysts synthesized by DI, a synthesis approach not weight loading limited.

3.2.1.2. Pd precursor. We studied the influence of the Pd precursor on the synthesis of the Pd-Zn γ-brass phase and the resulting Pd-Zn bimetallic particle size distribution. Tetraaminepalladium chloride was substituted for ammonium tetrachloropalladate to synthesize a 5% Pd/SiO_2 through DI (calcination-reduction according to Protocol 1) followed by the inclusion of Zn. XRD revealed the γ-brass phase is the only bimetallic phase present, while TEM analysis revealed there is no significant effect of Pd precursor on the particle size. Fig. 4 demonstrates the particle size distribution of the 5% Pd/SiO_2 and the corresponding Pd-Zn/SiO_2 samples synthesized using tetraaminepalladium chloride as the Pd precursor.

For the remainder of this sub-section, we utilize tetraaminepalladium chloride as the Pd precursor since a Pd cation (rather than anion) source is mandatory to impregnate SiO_2 at high pH by SEA [60]. Although, we demonstrated the choice of Pd precursor has no influence on the final particle size distribution of the bimetallic Pd-Zn, we opted to use the same precursor throughout the remainder of the parametric study to enable direct comparison between catalysts synthesized by the different methods.

3.2.1.3. Calcination-reduction protocol. We examined the influence of the calcination-reduction protocol on the size of the bimetallic Pd-Zn particles. As expected, we found the lower pretreatment temperatures in Protocol 2 (compared to Protocol 1) yielded smaller monometallic Pd particles in Step 1 and bimetallic Pd-Zn γ-brass particle after Step 2 (Fig. 4). The average Pd-Zn particle size from Protocol 2 is ~14 nm compared with ~25 nm for Protocol 1. Zn_2SiO_4 (willemite) diffraction peaks became much more prominent when Protocol 2 is used for the calcination-reduction of the parent Pd/SiO_2 compared to Protocol 1 (see below for more details) even though clear γ-brass peaks are visible (Figure S8). No other peaks (Pd, Zn, ZnO or Pd-Zn bimetallic phase) are identified in the diffractogram.

3.2.1.4. Method of Pd impregnation on SiO_2. As the final parametric variation in Step 1, we used SEA instead of DI to synthesize the parent Pd/SiO_2 catalyst. As previously mentioned, the nominal loading of Pd is 5 wt. %, tetraaminepalladium chloride is used as the Pd precursor and Protocol 2 is used for the calcination-reduction pretreatment. The particle size for the parent Pd/SiO_2 synthesized by SEA is ~ 6 nm. After the inclusion of Zn, we found the final average particle size increased to ~8 nm, a substantial reduction in particle size compared to DI-synthesized Pd/SiO_2 with a similar Pd loading.

XRD revealed the presence of distinct Zn_2SiO_4 (willemite) peaks as the only impurity phase (Figure S8), having similar intensity to the previous case (Step 1 – 5% Pd/SiO_2 material synthesized by DI and calcined and reduced according to Protocol 2 prior to Zn impregnation). STEM-EDS suggests Zn_2SiO_4 peaks originate from a few very large Zn_2SiO_4 particles formed on the support (Figure S8) during synthesis rather than an increase in the concentration of the finely dispersed Zn_2SiO_4 particles mentioned in Section 3.1.

Figs. 5a and b demonstrate the particle size distribution is much improved (with almost no agglomerated particles) compared to all previous syntheses. Fig. 5c demonstrates at the single particle level, the Pd:Zn ratio measured by STEM-EDS falls within the compositional bounds of the γ-brass phase. This further confirms Zn trapped as Zn_2SiO_4 represents a relatively small fraction of the total Zn (because we started with a stoichiometric amount of Zn) added, but appear as prominent peaks because of large particle size and the biased nature of XRD towards larger crystallite size.

The monometallic Pd particle size has a significant effect on the final bimetallic particle size. The final bimetallic particle size can be predicted based on simple mass balance arguments (Supporting Information section S2). However, there is a 5–20% discrepancy between theoretical and experimental values (Table S1) and the % discrepancy becomes more positive (theory overestimates actual value) at smaller particle size. At this point the exact reason for this behavior is unknown but it may arise from partial violation of our assumptions while calculating the theoretical value (particle is spherical and there are no crystal defects, see footnote “b” in Table S1). It is also noteworthy that our particle size distribution always has considerable spread (with a long ‘tail’ towards higher diameters compared to a Gaussian distribution) possibly due to high temperature agglomeration induced by the high temperatures required for Zn inclusion.

Optimal synthesis of monometallic NPs has been a focus of research for many years now and this experience can be directly translated into our synthesis approach to further optimize the average diameter and particle size distribution of bimetallic NPs. However, in this context, there is likely a particle size limit below which the γ-brass phase cannot be achieved. Calculations by Mukhopadhyay et al. [56] demonstrated the Cu_5Zn_8 γ-brass crystal structure is thermodynamically unfavorable (based on free energy of formation arguments [75]) below a crystallite size of 8 nm. We observed our synthetic approach is also sensitive to particle size. By SEA, we synthesized a parent 2.5% Pd/SiO_2 with an estimated (by CO chemisorption) average particle diameter of ~ 3 nm. Upon addition of a stoichiometric quantity of Zn to form the γ-brass phase and heating at 750 °C for 12 h, the XRD pattern revealed β-phase Pd-Zn was the only bimetallic phase present. Zn_2SiO_4 peaks were also detected but no unreacted monometallic Zn or Pd peaks could be identified. This observation is qualitatively consistent with the existing literature since the numerous approaches reported for the synthesis of

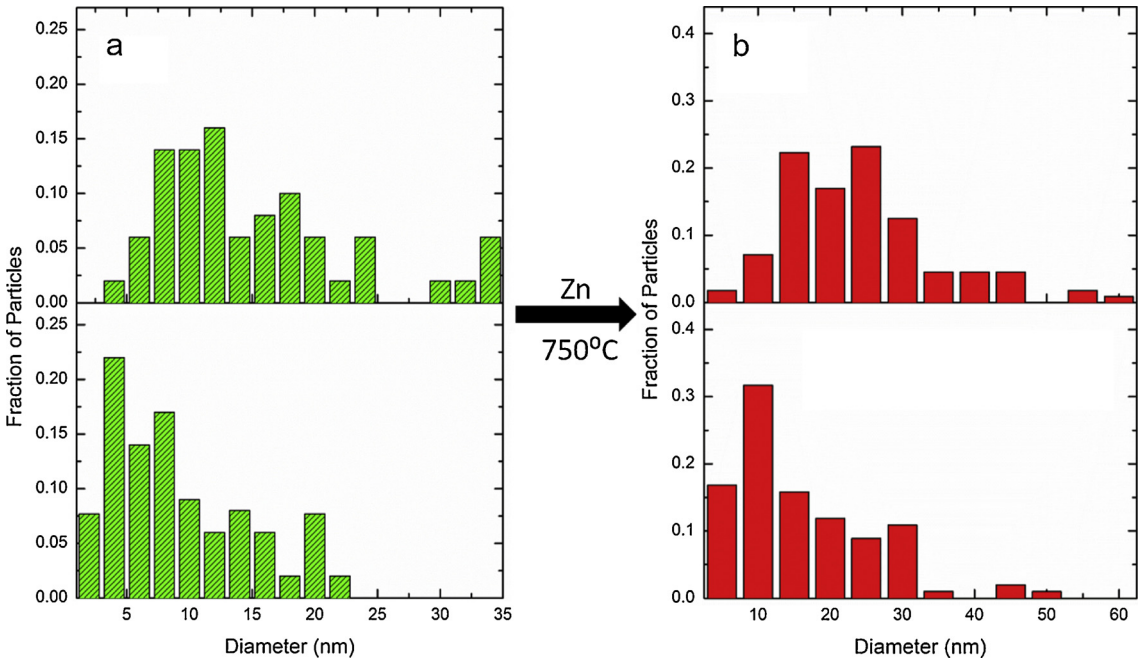

Fig. 4. (top) Particle size distribution for (a) 5% Pd/SiO_2 treated using Protocol 1 and (b) the corresponding Pd-Zn/SiO_2 γ-brass catalyst. (bottom) Particle size distribution for (a) 5% Pd/SiO_2 treated using Protocol 2 and (b) the corresponding Pd-Zn/SiO_2 γ-brass catalyst. The monometallic particle size histograms are colored green with black patterning while the bimetallic particle size histograms are colored solid red. (For interpretation of the references to colour in this figure legend, the reader is referred to the web version of this article.)

Pd-Zn invariably use small (sometimes even single atom) Pd particles and consistently form the β-phase even when sufficient Zn is provided to access the γ-brass phase (also see Section S1) [36,37,57,58]. It is also consistent with our observation that larger Zn_2SiO_4 agglomerates form as the diameter of the parent Pd particle (in Step 1) decreases below ~10 nm suggesting Zn integration into the Pd NPs is dependent upon Pd particle size. If the particle size is below a certain threshold diameter, the side reaction of Zn with the support begins to compete with the formation of the γ-brass phase.

3.2.2. Influence of vacuum heating (diffusion) time after Zn addition (Step 2)

In this section, we determine the mechanism of γ-brass phase formation and the time required to transform Pd/SiO_2 into the intermetallic Pd-Zn γ-brass phase. Two pathways (direct and sequential) are possible for the synthesis of the γ-brass phase.

Path 1: Pd + Zn → Pd-rich alloy (~Pd_3Zn) + Zn → β-phase (~Pd_1Zn_1) + Zn → γ-phase (~Pd_2Zn_{11})

Path 2: Pd + Zn → γ-phase

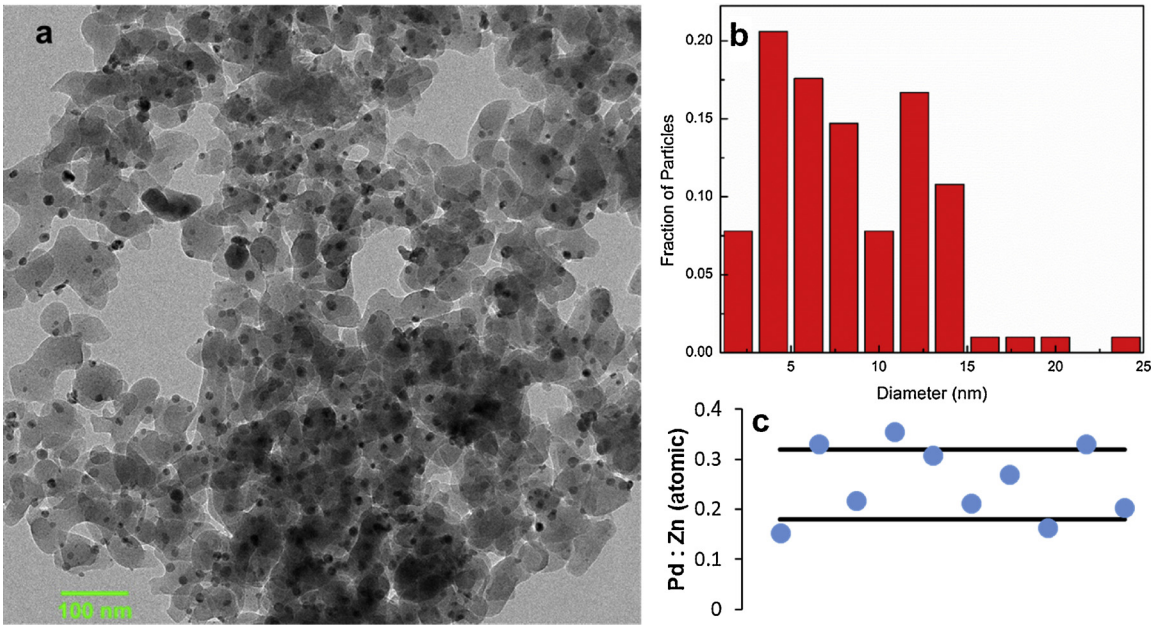

Fig. 5. (a) TEM image, (b) particle size distribution and (c) individual particle-by-particle STEM-EDS determined composition of γ-brass Pd-Zn/SiO_2 using the parent 5% Pd/SiO_2 synthesized by SEA. Black lines in (c) indicate the compositional bounds of the Pd-Zn γ-brass phase [47].

Since we require the ability to unequivocally identify the γ-brass phase and estimate its purity, we utilized the 9% Pd/SiO_2 sample (reported in Section 3.1) to ensure sharp and distinct XRD peaks can be identified and characterized. We used four different heating times (12 h, 6 h, 3 h and ½ h at a constant temperature of 750 °C) for the inclusion of Zn in Pd/SiO_2 (Step 2). Phase-pure γ-brass Pd-Zn NP formation was confirmed by XRD for the samples heated for 3–12 h. There does not appear to be any significant change in the peak shape due to the increased heating time (Fig. 6a), indicating 3 h is sufficient to obtain phase-pure γ-brass Pd-Zn NPs. For a heating time of ½ h, the peaks are distinctly broader (indicating crystal disorder/defect) but can still be indexed to the γ-brass phase. However, a ZnO peak is clearly visible as indicated in Fig. 6b. Considering the extreme oxophilic nature of Zn, this ZnO peak likely represents unconsumed metallic Zn which was oxidized upon exposure to ambient.

Fig. 6c shows the variation in the Pd:Zn ratio as a function of the time for high temperature (750 °C) Zn inclusion. The ICP-determined (blue points) Pd:Zn ratio increases (from a starting value of 0.19) with time, indicative of a small amount of Zn loss due to evaporation. The average composition (15–20 particles) of the bimetallic particles were also determined for the two extreme cases using STEM-EDS (red points)[1]. In the sample heated for 12 h, ICP and STEM-EDS determined compositions are nearly identical indicating most of the Zn is incorporated in the bimetallic particles leaving only a very small fraction of Zn to form silicates or oxides. However, for the sample heated only for a ½ h, there is a substantial difference between the composition determined by ICP-OES and STEM-EDS. The significantly higher Pd:Zn ratio (Fig. 6c) of the STEM-EDS (red data point) compared to the ICP (blue data point) indicates a substantial amount of Zn is present on the sample but not incorporated into the Pd NPs. Fig. 6d provides visual confirmation of two adjacent particles with very different composition. The particle on the left has a higher than average ICP-determined Pd:Zn ratio (but within the bounds of γ-brass phase), while the second particle contains no Pd and is likely ZnO. However, it should be noted that all points (red and blue) in Fig. 6c lies well within the compositional bounds of the γ-brass phase (15.4–24 at% Pd). The above experimental evidence, particularly given that solid-state high temperature diffusion is a rather slow process, suggests Path 2 is dominant. However, the kinetics appears to be too fast and does not allow us to rigorously study the synthesis mechanism by the current *ex-situ* approach.

The average particle size and the corresponding distribution for the 12 h and 1/2 h samples were examined by TEM. Interestingly, the time for high temperature Zn inclusion has little influence on particle size (Figure S9) of the γ-brass NPs indicating no significant sintering occurred during the high temperature Zn inclusion step (Step 2). Our results suggest the size of the NPs is solely determined by the initial size of the Pd/SiO_2 seed particles (Step 1) and there is a particle size threshold required for the formation of the γ-brass phase. The formation of the γ-brass phase is facile and can be completed within 3 h at 750 °C with high phase purity and crystallinity if the diameter of the initial monometallic Pd particle is above a threshold size.

3.3. Proof of catalytic active site modification after Zn inclusion

The combination of characterization techniques prove the inclusion of Zn into the supported Pd NPs results in a change in the bulk crystal structure of the NPs due to the formation of the γ-brass phase. In this section, we probe the effect of Zn inclusion on the catalytic behavior. The catalytic surface is first probed through a comparison of CO adsorption on the parent Pd/SiO_2 and the corresponding $Pd\text{-}Zn/SiO_2$ catalysts. The 5% Pd/SiO_2 catalyst synthesized by SEA and its corresponding γ-brass bimetallic were used for this study since they contain the smallest monometallic and bimetallic NPs, respectively. Fig. 7a and S10a demonstrates appreciable CO uptake on the monometallic catalyst. The particle size determined by chemisorption is estimated to be ~7.5 nm, in good agreement with our TEM determined particle size of 6 nm. The discrepancy may be attributed to our choice of 1:1 Pd:CO binding stoichiometry [65,76]. However, for $Pd\text{-}Zn/SiO_2$, we found negligible uptake of CO (Fig. 7a and S10b). This observation establishes Zn inclusion has significantly modified the catalytic active site. Previously Zhou et al. [36] and Meyer et al. [6] used DFT calculations to show the CO adsorption enthalpy decreases by ~100 kJ/mol on Pd-Zn (β-phase) compared to Pd. Experimental evidence also demonstrates chemisorbed CO desorbs from a Pd-Zn alloy surface at temperatures as low as −73 °C [77,78] compared to about 120 °C on Pd/SiO_2 [79]. Our material contains significantly more diluted (in Zn) Pd sites and much greater Pd site isolation (see EXAFS data in Table 1) than the Pd-Zn materials cited above and a complete suppression of CO adsorption may be considered strong evidence of surface alloying with respect to Pd (no Pd shell, no finely dispersed non-alloyed Pd NPs). However, this result does not confirm the presence of exposed surface Pd (a Zn or ZnO shell will give the exact same data for CO chemisorption).

We employed low temperature (< 45 °C) ethylene hydrogenation as a probe reaction to identify the presence of Pd on the surface of the intermetallic NPs. Ethylene hydrogenation is facile on Pd but not catalyzed by Zn (or ZnO) at low temperatures and serves as a highly sensitive probe to identify the presence of Pd on the catalyst surface. Further, ethylene hydrogenation is famously insensitive to nanoscale structure (particle size and shape) [80–82] and hence a kinetic comparison (turnover frequency (TOF) or apparent activation energy) between Pd/SiO_2 and $Pd\text{-}Zn/SiO_2$ can be directly interpreted as the effect of Zn alloying and isolation of Pd active sites in an inert Zn matrix. In our study, the Pd/SiO_2 material had to be severely diluted (~4000 ppm) to maintain differential conversion and it is likely that despite our best efforts some heterogeneity existed. Therefore we used Arrhenius plots (Fig. 7b) and apparent activation barriers (which are insensitive to metal loading, dispersion and catalyst amount) for comparison of the Pd and Pd-Zn materials (instead of TOF). On pure Pd, the apparent activation energy is 38 kJ/mol, consistent with literature [83]. In contrast, the Pd-Zn γ-brass catalyst has a barrier of 63 kJ/mol clearly indicating the catalytic capabilities of Pd are modified (rather than lost) with Zn inclusion. This modification is likely due to changes in the catalytic active site through geometric and electronic effects identified through XAS and XPS experiments [6].

The evidence presented above clearly establishes at least the academic utility of these materials in better understanding the effect of Zn inclusion and the role of Pd site-isolation in many commercially important catalytic reactions [16,32]. However, such specific catalytic studies are beyond the scope of this current paper.

4. Extension to additional γ-brass phases: Ni-Zn, Cu-Zn and Ir-Zn

Our two-step synthesis technique was extended to other catalytically relevant M-Zn systems with the ambition of synthesizing the corresponding γ-brass phase NPs. We used 9% Ni/SiO_2 (d ~ 48 nm) or Cu/SiO_2 (d ~ 38 nm, DI, Protocol 1) as the Step 1 material. The synthesis was successful for both Ni-Zn and Cu-Zn as the γ-brass phase was the only bimetallic phase formed with a very small amount of Zn_2SiO_4 identified as an impurity in Ni-Zn (Fig. 8a). The average particle size was significantly larger compared to the corresponding Pd-Zn case (as discussed in Section 3.1). For Cu-Zn, the particle size was estimated to be ~50 nm, while for Ni-Zn, the particle size was ~100 nm (Fig. 8b–d). It is evident that while our synthesis technique can be directly extended to other transition metals, its performance (in terms of

[1] ICP considers all of the Zn present in the sample irrespective of its oxidation state (metallic or Zn^{2+}). Zn which has escaped the crucible as Zn vapor is not accounted for by ICP-OES. STEM-EDS elemental quantification has been done exclusively for the bimetallic particles and does not consider Zn in Zn^{2+} or pure metal form present on the support due to either incomplete alloying or parallel Zn_2SiO_4 or ZnO formation.

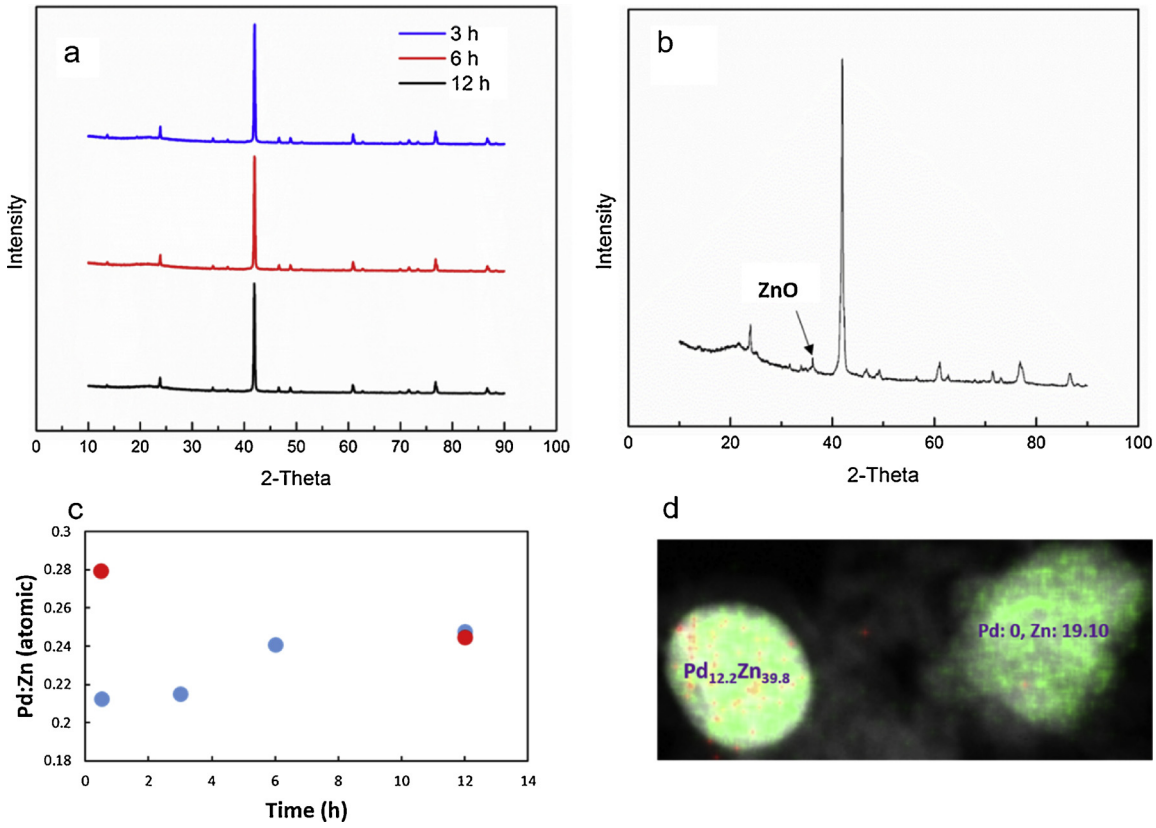

Fig. 6. (a) XRD pattern after different Zn diffusion times at 750 °C during Step 2. All sharp features correspond to the Pd-Zn γ-brass phase. (b) XRD pattern after heating for ½ h at 750 °C. The peaks are broader than in (a) and a distinct ZnO peak is observed. (c) Effect of Zn diffusion time (at 750 °C) on average composition measured by ICP (blue) and STEM-EDS (red). During STEM-EDS only bimetallic particles are considered. The starting Pd:Zn ratio in each case was 0.19. The y-axis range shown in the plot corresponds to the γ-brass composition window. (d) STEM-EDS (red = Pd, green = Zn) of adjacent Pd-rich γ-brass bimetallic and Pd-free ZnO NPs after Zn inclusion for a ½ h at 750 °C. (For interpretation of the references to colour in this figure legend, the reader is referred to the web version of this article.)

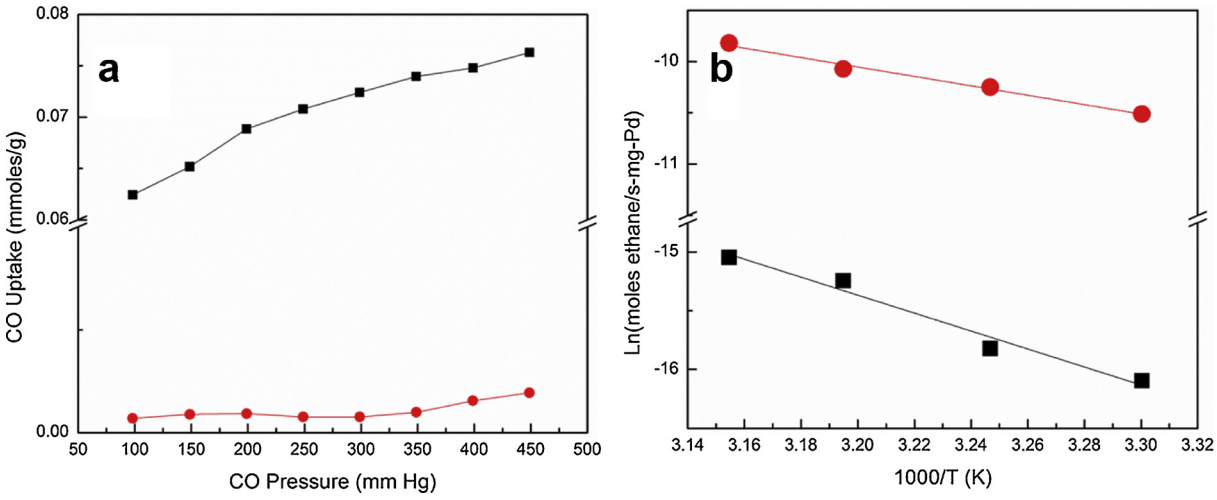

Fig. 7. (a) Irreversible CO chemisorption on 5% Pd/SiO_2 (SEA, Protocol 2, black squares) and the corresponding γ-brass intermetallic NPs (red circles). (b) Arrhenius plots for ethylene hydrogenation on 5% Pd/SiO_2 (red circle) and the corresponding $Pd\text{-}Zn/SiO_2$ γ-brass phase catalyst (black squares). Reaction mixture was 250 Torr ethylene, 250 Torr hydrogen and balance helium. The data point at 40^0C (1000/T = 3.19) was repeated in each case and the error was within 3% (~0.1% in terms of absolute conversion) between the first and repeat point and cannot be distinguished on the plot. (For interpretation of the references to colour in this figure legend, the reader is referred to the web version of this article.)

generating smaller NPs) is by far the best for Pd. It should also be noted extension to γ-brass Ni-Zn and Cu-Zn is intended to demonstrate the versatility of our approach and no efforts have been made to optimize the synthesis of Ni-Zn and Cu-Zn NPs. It is quite conceivable significantly smaller Cu or Ni-Zn γ-brass materials may be synthesized through approaches discussed in Section 3.

As a final example, we attempted to synthesize the Ir-Zn γ-brass phase, which is a line compound (Ir_2Zn_{11}) [50,84]. For our particular synthesis technique (using 5% Ir/SiO_2) we found a small amount of an Ir-Zn γ-brass phase formed but the majority of the Zn preferred to form Zn_2SiO_4 (Figure S11). Most of the Ir remained in metallic form as qualitatively determined by XRD. It appears our simple and novel 2-

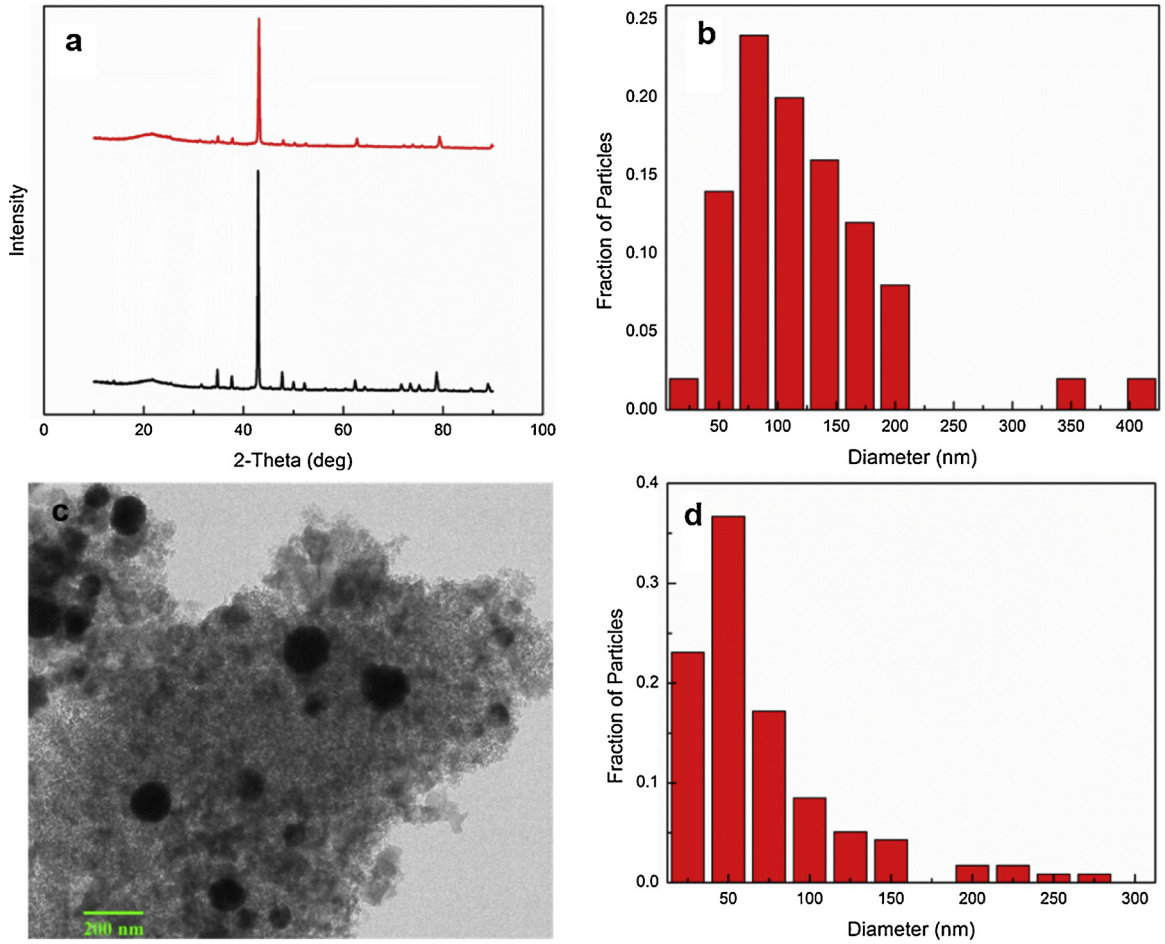

Fig. 8. (a) XRD patterns of SiO_2 supported Ni-Zn (black) and Cu-Zn (red) γ-brass phase containing ~9% Ni or Cu. (b) Particle size distribution and (c) TEM image of the Ni-Zn/SiO_2 material. (d) Particle size distribution of the Cu-Zn/SiO_2 material. (For interpretation of the references to colour in this figure legend, the reader is referred to the web version of this article.)

step synthesis approach can be generalized for several transition state metals (Pd, Ni and Cu) but is still not a universal technique for the synthesis of every M-Zn γ-brass phase (Fig. 1).

5. Conclusion

We developed a generalized synthesis technique for accessing M-Zn (M = Pd, Cu and Ni) γ-brass phase NPs supported on SiO_2. Willemite (Zn_2SiO_4) is the only impurity detected and no other bimetallic (or pure metal) phases formed (remained) during the transformation of supported M/SiO_2 to γ-brass M-Zn/SiO_2 by inclusion of Zn in Pd through high temperature bulk diffusion. Phase identification was confirmed by both XRD and electron microscopy (TEM + STEM-EDS). We tested several variables to optimize the synthetic procedure for SiO_2-supported Pd-Zn γ-brass NPs and conclude the final bimetallic particle size is controlled by the size of the Pd particle in the parent Pd/SiO_2 catalyst rather than the high temperature Zn inclusion step. The smallest particle size reported here (~8 nm) is comparable to the state-of-the-art for similar bimetallic systems [16]. Although our approach was successful for Pd-Zn, Cu-Zn and Ni-Zn, suggesting a general approach to supported γ-brass nanoparticles, we found the synthesis of the line compound, γ-brass Ir-Zn of low yield, demonstrating the proposed hybrid approach requires optimization for each M-Zn system. The choice of M also has a strong effect on the bimetallic particle size distribution with Pd yielding the highest dispersion. We demonstrate γ-brass Pd-Zn/SiO_2 is active for the low temperature hydrogenation of ethylene even though the CO adsorption capacity of the parent Pd/SiO_2 catalyst is significantly suppressed by the inclusion of Zn. Future prospects for intermetallic γ-brass NP catalysts include selective hydrogenation, formic acid decomposition and the oxygen reduction reaction due to favorable geometric and electronic properties of the γ-brass phase.

Acknowledgements

We acknowledge the US National Science Foundation (NSF grant # CBET – 1748365) for financial support of this work. This research used resources of the Advanced Photon Source, a U.S. Department of Energy (DOE) Office of Science User Facility operated for the DOE Office of Science by Argonne National Laboratory under Contract No. DE-AC02-06CH11357 (GUP 58386 and PUP-56176). We would also like to acknowledge the Material Characterization Laboratory's shared user facility at The Pennsylvania State University and staff scientists Dr. Jennifer Grey and Dr. Jeffrey Shallenberger for assistance with TEM indexing and XPS data collection and analysis, respectively.

Appendix A. Supplementary data

Supplementary data associated with this article can be found, in the online version, at https://doi.org/10.1016/j.cattod.2018.10.050.

References

[1] G.A. Somorjai, Y.G. Borodko, Research in nanosciences – great opportunity for catalysis science, Catal. Lett. 76 (2001) 1–5.
[2] N. Lopez, C. Vargas-Fuentes, Promoters in the hydrogenation of alkynes in mixtures:

insights from density functional theory, Chem. Commun. 48 (2012) 1379–1391.
[3] J.K. Norskov, T. Bligaard, J. Rossmeisl, C.H. Christensen, Towards the computational design of solid catalysts, Nat. Chem. 1 (2009) 37–46.
[4] S. Furukawa, T. Komatsu, Selective hydrogenation of functionalized alkynes to (E)-alkenes, using ordered alloys as catalysts, ACS Catal. 6 (2016) 2121–2125.
[5] T. Komatsu, S. Furukawa, Intermetallic compound nanoparticles dispersed on the surface of oxide support as active and selective catalysts, Mater. Trans. 56 (2015) 460–467.
[6] R.J. Meyer, Q. Zhang, A. Kryczka, C. Gomez, R. Todorovic, Perturbation of Reactivity with Geometry: How Far Can We Go? ACS Catal. 8 (2018) 566–570.
[7] J.H. Sinfelt, Catalysis by alloys and bimetallic clusters, Acc. Chem. Res. 10 (1977) 15–20.
[8] T. Cheng, X.-Y. Lang, G.-F. Han, R.-Q. Yao, Z. Wen, Q. Jiang, Nanoporous (Pt1-xFex) 3Al intermetallic compounds for greatly enhanced oxygen electroreduction catalysis, J. Mater. Chem. A 4 (2016) 18878–18884.
[9] G.-F. Han, L. Gu, X.-Y. Lang, B.-B. Xiao, Z.-Z. Yang, Z. Wen, Q. Jiang, Scalable nanoporous (Pt1–xNix)3Al intermetallic compounds as highly active and stable catalysts for oxygen electroreduction, ACS Appl. Mater. Interfaces 8 (2016) 32910–32917.
[10] Y. Jiang, Y. He, C.T. Liu, Review of porous intermetallic compounds by reactive synthesis of elemental powders, Intermetallics (2017).
[11] X.Y. Lang, G.F. Han, B.B. Xiao, L. Gu, Z.Z. Yang, Z. Wen, Y.F. Zhu, M. Zhao, J.C. Li, Q. Jiang, Mesostructured intermetallic compounds of platinum and non-transition metals for enhanced electrocatalysis of oxygen reduction reaction, Adv. Funct. Mater. 25 (2015) 230–237.
[12] B. Qiao, A. Wang, X. Yang, L.F. Allard, Z. Jiang, Y. Cui, J. Liu, J. Li, T. Zhang, Single-atom catalysis of CO oxidation using Pt1/FeOx, Nat. Chem. 3 (2011) 634–641.
[13] J.S. Sun, Z. Wen, L.P. Han, Z.W. Chen, X.Y. Lang, Q. Jiang, Nonprecious intermetallic Al7Cu4Ni nanocrystals seamlessly integrated in freestanding bimodal nanoporous copper for efficient hydrogen evolution catalysis, Adv. Funct. Mater. 28 (2018) 1706127.
[14] Y.-J. Wang, N. Zhao, B. Fang, H. Li, X.T. Bi, H. Wang, Carbon-supported Pt-Based alloy electrocatalysts for the oxygen reduction reaction in polymer electrolyte membrane fuel cells: particle size, shape, and composition manipulation and their impact to activity, Chem. Rev. 115 (2015) 3433–3467.
[15] D.G. Xia, G. Chen, Z.Y. Wang, J.J. Zhang, S.Q. Hui, D. Ghosh, H.J. Wang, Synthesis of ordered intermetallic PtBi2 nanoparticles for methanol-tolerant catalyst in oxygen electroreduction, Chem. Mater. 18 (2006) 5746–5749.
[16] A. Dasgupta, R.M. Rioux, Intermetallics in catalysis: an exciting subset of multimetallic catalysts, Catal. Today (2018).
[17] D.B. Tiedtke, J.J. Bergmeister, P. Cheung, R.A. Rhoades, Progress in the Development of E-series Catalyst Technologies for the Selective Hydrogenation of Acetylene in Various Hydrocarbon Streams, Chevron Phillips Chemical Company, 2001.
[18] C. Li, Y. Chen, S. Zhang, J. Zhou, F. Wang, S. He, M. Wei, D.G. Evans, X. Duan, Nickel-Gallium intermetallic nanocrystal catalysts in the semihydrogenation of phenylacetylene, ChemCatChem 6 (2014) 824–831.
[19] K. Schutte, A. Doddi, C. Kroll, H. Meyer, C. Wiktor, C. Gemel, G. van Tendeloo, R.A. Fischer, C. Janiak, Colloidal nickel/gallium nanoalloys obtained from organometallic precursors in conventional organic solvents and in ionic liquids: noble-metal-free alkyne semihydrogenation catalysts, Nanoscale 6 (2014) 5532–5544.
[20] Y. Liu, X. Liu, Q. Feng, D. He, L. Zhang, C. Lian, R. Shen, G. Zhao, Y. Ji, D. Wang, G. Zhou, Y. Li, Intermetallic NixMy (M = Ga and Sn) nanocrystals: a non-precious metal catalyst for semi-hydrogenation of Alkynes, Adv. Mater. 28 (2016) 4747–4754.
[21] F. Studt, I. Sharafutdinov, F. Abild-Pedersen, C.F. Elkjær, J.S. Hummelshøj, S. Dahl, I. Chorkendorff, J.K. Nørskov, Discovery of a Ni-Ga catalyst for carbon dioxide reduction to methanol, Nat. Chem. 6 (2014) 320–324.
[22] D.A. Torelli, S.A. Francis, J.C. Crompton, A. Javier, J.R. Thompson, B.S. Brunschwig, M.P. Soriaga, N.S. Lewis, Nickel–gallium-catalyzed electrochemical reduction of CO2 to highly reduced products at low overpotentials, ACS Catal. 6 (2016) 2100–2104.
[23] P. Natarajan, H.A. Khan, S. Yoon, K.-D. Jung, One-pot synthesis of Pt–Sn bimetallic mesoporous alumina catalysts with worm-like pore structure for n-butane dehydrogenation, J. Ind. Eng. Chem. 63 (2018) 380–390.
[24] L. Sun, Y. Chai, W. Dai, G. Wu, N. Guan, L. Li, Oxidative dehydrogenation of propane over Pt–Sn/Si-beta catalysts: key role of Pt–Sn interaction, Catal. Sci. Technol. 8 (2018) 3044–3051.
[25] Q. Li, Z. Sui, X. Zhou, D. Chen, Kinetics of propane dehydrogenation over Pt–Sn/Al2O3 catalyst, Appl. Catal. A Gen. 398 (2011) 18–26.
[26] E. Casado-Rivera, Z. Gál, A.C.D. Angelo, C. Lind, F.J. DiSalvo, H.D. Abruña, Electrocatalytic oxidation of formic acid at an ordered intermetallic PtBi surface, ChemPhysChem 4 (2003) 193–199.
[27] X. Ji, K.T. Lee, R. Holden, L. Zhang, J. Zhang, G.A. Botton, M. Couillard, L.F. Nazar, Nanocrystalline intermetallics on mesoporous carbon for direct formic acid fuel cell anodes, Nat. Chem. 2 (2010) 286.
[28] L.J. Zhang, Z.Y. Wang, D.G. Xia, Bimetallic PtPb for formic acid electro-oxidation, J. Alloys. Compd. 426 (2006) 268–271.
[29] L.R. Alden, D.K. Han, F. Matsumoto, H.D. Abruna, F.J. DiSalvo, Intermetallic PtPb nanoparticles prepared by sodium naphthalide reduction of metal-organic precursors: electrocatalytic oxidation of formic acid, Chem. Mater. 18 (2006) 5591–5596.
[30] E. Antolini, Alloy vs. Intermetallic compounds: effect of the ordering on the electrocatalytic activity for oxygen reduction and the stability of low temperature fuel cell catalysts, Appl. Catal. B 217 (2017) 201–213.
[31] E. Antolini, J.R.C. Salgado, M.J. Giz, E.R. Gonzalez, Effects of geometric and electronic factors on ORR activity of carbon supported Pt–Co electrocatalysts in PEM fuel cells, Int. J. Hydrogen Energy 30 (2005) 1213–1220.
[32] M. Armbrüster, M. Behrens, K. Föttinger, M. Friedrich, É. Gaudry, S.K. Matam, H.R. Sharma, The intermetallic compound ZnPd and its role in methanol steam reforming, Catal. Rev. 55 (2013) 289–367.
[33] B.E. Green, C.S. Sass, L.T. Germinario, P.S. Wehner, B.L. Gustafson, Ester hydrogenation over Pd-Zn/SiO2, J. Catal. 140 (1993) 406–417.
[34] M.L. Cubeiro, J.L.G. Fierro, Partial oxidation of methanol over supported palladium catalysts, Appl. Catal. A Gen. 168 (1998) 307–322.
[35] N. Iwasa, T. Mayanagi, N. Ogawa, K. Sakata, N. Takezawa, New catalytic functions of Pd–Zn, Pd–Ga, Pd–In, Pt–Zn, Pt–Ga and Pt–In alloys in the conversions of methanol, Catal. Letters 54 (1998) 119–123.
[36] H. Zhou, X. Yang, L. Li, X. Liu, Y. Huang, X. Pan, A. Wang, J. Li, T. Zhang, PdZn intermetallic nanostructure with Pd-Zn-Pd ensembles for highly active and chemoselective semi-hydrogenation of acetylene, ACS Catal. (2015) 1054–1061.
[37] A. Sarkany, Z. Zsoldos, B. Furlong, J.W. Hightower, L. Guczi, Hydrogenation of 1-Butene and 1,3-Butadiene Mixtures over Pd/ZnO Catalysts, J. Catal. 141 (1993) 566–582.
[38] C.S. Spanjers, J.T. Held, M.J. Jones, D.D. Stanley, R.S. Sim, M.J. Janik, R.M. Rioux, Zinc inclusion to heterogeneous nickel catalysts reduces oligomerization during the semi-hydrogenation of acetylene, J. Catal. 316 (2014) 164–173.
[39] A.H. Al-ShaikhAli, A. Jedidi, D.H. Anjum, L. Cavallo, K. Takanabe, Kinetics on NiZn bimetallic catalysts for hydrogen evolution via selective dehydrogenation of methylcyclohexane to toluene, ACS Catal. 7 (2017) 1592–1600.
[40] A.T. Hanindriyo, T.B.M.Y.Y. Prawira, M.K. Agusta, R. Maezono, H.K. Dipojono, Computational design of Ni-Zn based catalyst for direct hydrazine fuel cell catalyst using density functional theory, Procedia Eng. 170 (2017) 148–153.
[41] X. Kong, Y. Zhu, H. Zheng, Y. Zhu, Z. Fang, Inclusion of Zn into metallic Ni enables selective and effective synthesis of 2,5-dimethylfuran from bioderived 5-Hydroxymethylfurfural, ACS Sustain. Chem. Eng. 5 (2017) 11280–11289.
[42] A. Miura, H. Wang, B.M. Leonard, H.D. Abruña, F.J. DiSalvo, Synthesis of intermetallic PtZn nanoparticles by reaction of Pt nanoparticles with Zn vapor and their application as fuel cell catalysts, Chem. Mater. 21 (2009) 2661–2667.
[43] Q. Feng, S. Zhao, Y. Wang, J. Dong, W. Chen, D. He, D. Wang, J. Yang, Y. Zhu, H. Zhu, L. Gu, Z. Li, Y. Liu, R. Yu, J. Li, Y. Li, Isolated single-atom Pd sites in intermetallic nanostructures: high catalytic selectivity for semihydrogenation of Alkynes, J. Am. Chem. Soc. 139 (2017) 7294–7301.
[44] C.S. Spanjers, R.S. Sim, N.P. Sturgis, B. Kabius, R.M. Rioux, In situ spectroscopic characterization of Ni1– x znx ZnO catalysts and their selectivity for acetylene semihydrogenation in excess ethylene, ACS Catal. 5 (2015) 3304–3315.
[45] S. Jana, J.W. Chang, R.M. Rioux, Synthesis and modeling of hollow intermetallic Ni–Zn nanoparticles formed by the kirkendall effect, Nano Lett. 13 (2013) 3618–3625.
[46] D.-M. Rao, S.-T. Zhang, C.-M. Li, Y.-D. Chen, M. Pu, H. Yan, M. Wei, The reaction mechanism and selectivity of acetylene hydrogenation over Ni–Ga intermetallic compound catalysts: a density functional theory study, J. Chem. Soc. Dalton Trans. 47 (2018) 4198–4208.
[47] H. Okamoto, Phase Diagrams of Binary Alloys, ASM International, 2010.
[48] A.J. Bradley, J. Thewlis, The structures of Gamma Brass, Proc. Roy. Soc. 112 (1926) 678–692.
[49] C.S. Spanjers, A. Dasgupta, M. Kirkham, B.A. Burger, G. Kumar, M.J. Janik, R.M. Rioux, Determination of bulk and surface atomic arrangement in Ni–Zn γ-Brass phase at different Ni to Zn ratios, Chem. Mater. 29 (2017) 504–512.
[50] L. Arnberg, S. Westman, Note on the structure of the gamma brass like phase Ir4Zn22, Acta Chem. Scand. 26 (1972) 513–517.
[51] V.-A. Edstrom, S. Westman, X-Ray determination of the structure of cubic gamma Pd,Zn phase, Acta Chem. Scand. 23 (1969) 279–285.
[52] O.a.J.A.a.W.S. Heidenstam, A Redetermination of the Distribution of Atoms inCu5Zn8, Cu5Cd8, and Cu9Al4, Acta Chemica Scandinavica, 22 (1968) 653–661.
[53] A. Johansson, H. Ljung, S. Westman, X-Ray and Neutron Diffraction Studies on gamma-Ni,Zn and gamma-Fe,Zn, (1968), pp. 2743–2753.
[54] K. Kovnir, M. Armbrüster, D. Teschner, T.V. Venkov, F.C. Jentoft, A. Knop-Gericke, Y. Grin, R. Schlögl, A new approach to well-defined, stable and site-isolated catalysts, Sci. Technol. Adv. Mater. 8 (2007) 420–427.
[55] R.E. Cable, R.E. Schaak, Solution synthesis of nanocrystalline m − Zn (M = Pd, Au, Cu) intermetallic compounds via chemical conversion of metal nanoparticle precursors, Chem. Mater. 19 (2007) 4098–4104.
[56] N.K. Mukhopadhyay, D. Mukherjee, S. Bera, I. Manna, R. Manna, Synthesis and characterization of nano-structured Cu–Zn γ-brass alloy, Mater. Sci. Eng. A (2008).
[57] D.J. Childers, N.M. Schweitzer, S.M.K. Shahari, R.M. Rioux, J.T. Miller, R.J. Meyer, Modifying structure-sensitive reactions by addition of Zn to Pd, J. Catal. 318 (2014) 75–84.
[58] S. Wang, K. Gao, W. Li, J. Zhang, Effect of Zn addition on the direct synthesis of hydrogen peroxide over supported palladium catalysts, Appl. Catal. A Gen. 531 (2017) 89–95.
[59] A. Onda, T. Komatsu, T. Yashima, Preparation and catalytic properties of single-phase Ni–Sn intermetallic compound particles by CVD of Sn(CH3)4 onto Ni/Silica, J. Catal. 201 (2001) 13–21.
[60] L. Jiao, J.R. Regalbuto, The synthesis of highly dispersed noble and base metals on silica via strong electrostatic adsorption: I. Amorphous silica, J. Catal. 260 (2008) 329–341.
[61] O. Heidenstam, A. Johansson, S. Westman, A redetermination of the distribution of atoms inCu5Zn8, Cu5Cd8, and Cu9Al4, Acta Chem. Scand. 22 (1968) 653–661.
[62] O. Gourdon, D. Gout, D.J. Williams, T. Proffen, S. Hobbs, G.J. Miller, Atomic Distributions in the Γ-brass structure of the Cu-Zn System: a Structural and Theoretical Study, J. Biol. Inorg. Chem. 46 (2006) 251–260.

[63] O. Gourdon, Z. Izaola, L. Elcoro, V. Petricek, G.J. Miller, Structure determination of two modulated γ-Brass structures in the Zn − Pd System through a (3 + 1)-dimensional space description, Inorg. Chem. 48 (2009) 9715–9722.
[64] J. Schindelin, I. Arganda-Carreras, E. Frise, V. Kaynig, M. Longair, T. Pietzsch, S. Preibisch, C. Rueden, S. Saalfeld, B. Schmid, J.-Y. Tinevez, D.J. White, V. Hartenstein, K. Eliceiri, P. Tomancak, A. Cardona, Fiji: an open-source platform for biological-image analysis, Nat Meth 9 (2012) 676–682.
[65] M. Boudart, G. Djega-Mariadassou, Kinetics of Heterogenous Catalytic Reactions, Princeton Univeristy Press, 1984.
[66] B. Ravel, ATOMS: crystallography for the X-ray absorption spectroscopist, J. Synchrotron Radiat. 8 (2001) 314–316.
[67] B. Ravel, M. Newville, Athena, artemis, hephaestus: data analysis for X-ray absorption spectroscopy using IFEFFIT, J. Synchrotron Radiat. 12 (2005) 537–541.
[68] M.P. Seah, Summary of ISO/TC 201 Standard: VII ISO 15472 : 2001—surface chemical analysis—x-ray photoelectron spectrometers—calibration of energy scales, Surf. Interface Anal. 31 (2001) 721–723.
[69] N. Schweitzer, H. Xin, E. Nikolla, J.T. Miller, S. Linic, Establishing relationships between the geometric structure and chemical reactivity of alloy catalysts based on their measured electronic structure, Top. Catal. 53 (2010) 348–356.
[70] N. Kopfle, L. Mayr, P. Lackner, M. Schmid, D. Schidmair, T. Gotsch, S. Penner, B. Kloetzer, Zirconium-palladium interactions during dry reforming of methane, ECS Trans. 78 (2017) 2419–2430.
[71] C. Rameshan, W. Stadlmayr, S. Penner, H. Lorenz, L. Mayr, M. Hävecker, R. Blume, T. Rocha, D. Teschner, A. Knop-Gericke, R. Schlögl, D. Zemlyanov, N. Memmel, B. Klötzer, In situ XPS study of methanol reforming on PdGa near-surface intermetallic phases, J. Catal. 290 (2012) 126–137.
[72] F. Tao, M.E. Grass, Y. Zhang, D.R. Butcher, J.R. Renzas, Z. Liu, J.Y. Chung, B.S. Mun, M. Salmeron, G.A. Somorjai, Reaction-driven restructuring of Rh-Pd and Pt-Pd core-shell nanoparticles, Science 322 (2008) 932–934.
[73] F. Tao, M. Salmeron, In situ studies of chemistry and structure of materials in reactive environments, Science 331 (2011) 171–174.
[74] J.F. Moulder, W.F. Stickle, P.E. Sobol, K.D. Bomben, Handbook of X-ray Photoelectron Spectroscopy, Perkin-Elmer Corporation, 1992.
[75] A.K. Niessen, A.R. Miedema, F.R. de Boer, R. Boom, Enthalpies of formation of liquid and solid binary alloys based on 3d metals: IV. Alloys of cobalt, Phys. B + c 151 (1988) 401–432.
[76] P. Canton, G. Fagherazzi, M. Battagliarin, F. Menegazzo, F. Pinna, N. Pernicone, Pd/CO average chemisorption stoichiometry in highly dispersed supported Pd/γ-Al2O3 catalysts, Langmuir 18 (2002) 6530–6535.
[77] P. Pfeifer, K. Schubert, M.A. Liauw, G. Emig, PdZn catalysts prepared by wash-coating microstructured reactors, Appl. Catal. A Gen. 270 (2004) 165–175.
[78] J.A. Rodriguez, Interactions in bimetallic bonding: electronic and chemical properties of PdZn surfaces, J. Phys. Chem. 98 (1994) 5758–5764.
[79] H. Dropsch, M. Baerns, CO adsorption on supported Pd catalysts studied by adsorption microcalorimetry and temperature programmed desorption, Appl. Catal. A Gen. 158 (1997) 163–183.
[80] R.M. Rioux, R. Komor, H. Song, J.D. Hoefelmeyer, M. Grass, K. Niesz, P. Yang, G.A. Somorjai, Kinetics and mechanism of ethylene hydrogenation poisoned by CO on silica-supported monodisperse Pt nanoparticles, J. Catal. 254 (2008) 1–11.
[81] R.M. Rioux, H. Song, J.D. Hoefelmeyer, P. Yang, G.A. Somorjai, High surface area catalyst design: synthesis characterization, and reaction of platinum nano particles in mesoporous SBA-15 silica, J. Phys. Chem. B 109 (2005) 2192–2202.
[82] R.D. Cortright, S.A. Goddard, J.E. Rekoske, J.A. Dumesic, Kinetic study of ethylene hydrogenation, J. Catal. 127 (1991) 342–353.
[83] H. Molero, D. Stacchiola, W.T. Tysoe, The kinetics of ethylene hydrogenation catalyzed by metallic palladium, Catal. Lett. 101 (2005) 145–149.
[84] W. Hornfeck, S. Thimmaiah, S. Lee, B. Harbrecht, Structure–composition relations for the partly disordered hume-Rothery Phase Ir7 + 7δZn97 − 11δ (0.31 ≤ δ ≤ 0.58), Chem. Eur. J. 10 (2004) 4616–4626.